Continental Shelf Parameters Inferred from SAR Internal Wave Observations

D. L. PORTER AND D. R. THOMPSON

The Johns Hopkins University, Applied Physics Laboratory, Laurel, Maryland

(Manuscript received 23 July 1997, in final form 12 May 1998)

ABSTRACT

This paper presents preliminary results on the use of synthetic aperture radar (SAR) imagery to extract oceanographic information about the continental shelf. From late spring through early fall the thermocline on the shelf is fully developed and the entire Mid-Atlantic Bight is replete with internal waves. The surface manifestation of these internal waves is observed using the SAR on board the *European Research Satellite-1*. The depth of the pycnocline and the density of the surface layer can be estimated from the dispersion relation obtained from a two-layer fluid model. The other parameters that are required to make this estimate are obtained by assuming climatological bottom density, estimating the speed of propagation from the tidal-generated wave packets, and calculating the depth of the pycnocline based on the isobath where the internal waves are dissipated. This robust method for obtaining quantitative information about the structure of the shelf's water column shows good agreement with the in situ observations from that area.

1. Introduction

During the late spring, summer, and early fall, when the thermocline is fully developed, much of the continental shelf waters of the entire North American continent are replete with internal waves. Surface manifestations of internal waves in the shallow continental shelf waters have been observed in Massachusetts Bay and along the Virginia coast as well as along the West Coast of the United States. Their surface signatures have been observed from ships (Gotwols et al. 1988), from aircraft (Gasparovic et al. 1988), from moored instruments (Liu 1988), and from manned and unmanned spacecraft (Porter and Thompson 1996). In situ measurements are often used to estimate the parameters of the remotely observed internal wave's surface effects, and model studies (Thompson et al. 1988) have shown that the physics that govern the generation of these effects is reasonably well understood. Our goal in the present paper is to investigate the possibility of using the remotely observed surface manifestation of these internal waves to infer the structure of the water properties on the continental shelf.

One of the sites where internal waves have received much study is the Mid-Atlantic Bight, situated between Long Island, New York, and the New Jersey coast. For example, the synthetic aperture radar (SAR) Internal Wave Signature Experiment (SARSEX) was conducted in the New York Bight area southeast of Long Island in August 1984 (Gasparovic et al. 1988). In this experiment it was attempted for the first time to relate quantitatively in situ measurements of the internal wave field, stratification of the water column, and local meteorological conditions to the intensity modulations observed in the microwave SAR imagery.

During the summer of 1992 a Joint U.S.–Russia Internal Wave Experiment (JUSREX) took place in the waters off Long Island (Gasparovic 1992). The goals of this experiment were similar to those of SARSEX except the latter included more aircraft passes so that the wave's genesis, propagation, and dissipation across the shelf could be followed and studied. Concurrent with the experiment were overpasses of the *European Research Satellite-1* (*ERS-1*). On 18 July 1992 the SAR on board the satellite imaged two 100 km $\times$ 100 km overlapping scenes off Long Island. Figure 1 shows the two scenes (northern and southern) drawn on a chart of the area. The 200-m isobath line on the figure denotes the location of the shelf break, with the shallow shelf waters inshore and the deep abyss seaward of the line. The bathymetric feature in the southern image is Hudson Canyon.

Figure 2 shows the changes in the density stratification that occur during the seasonal cycle at a site located at 39°39′N, 72°46′W on the shelf (at the position of the asterisk in Fig. 1). These data are from the Marine Resources Monitoring, Assessment, and Prediction (MARMAP) Program (Manning and Holzwarth 1990) collected by NOAA between 1977 and 1985. During the winter and early spring (January, February, and April), the water column is well mixed with a sigma-*T* value around 26, caused by the cold winds from winter

Corresponding author address: Dr. David L. Porter, Applied Physics Laboratory, Johns Hopkins University, Johns Hopkins Road, Laurel, MD 20723-6099.
E-mail: David.Porter@jhuapl.edu

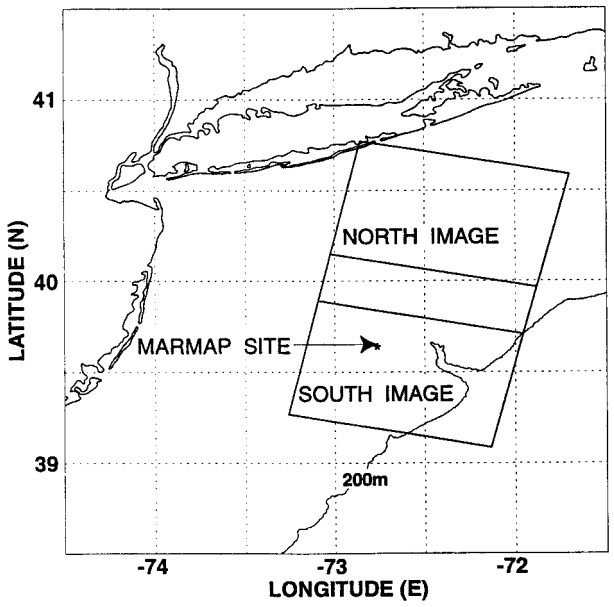

FIG. 1. Location of two overlapping SAR images collected on 18 July 1992 off the coast of Long Island. The 200-m isobath shows the location of the Hudson Canyon located near the center of the southern image, and the asterisk shows were the MARMAP observations were made.

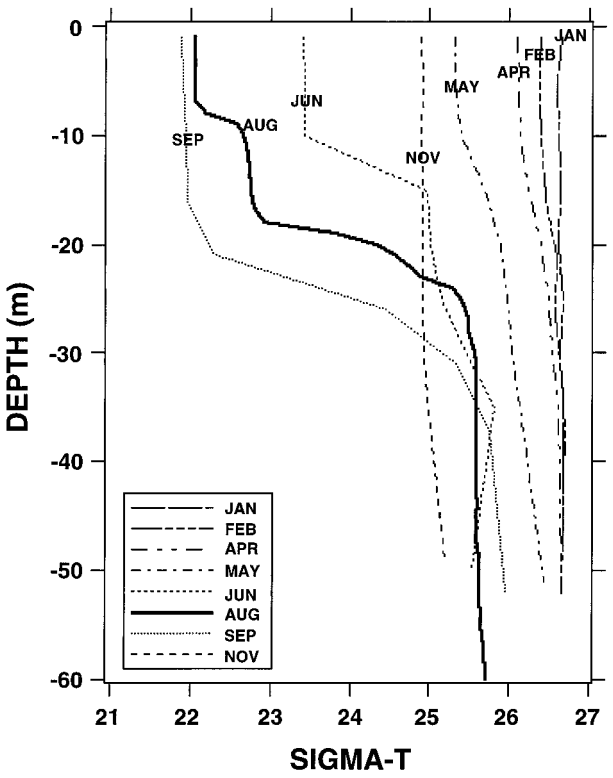

FIG. 2. Sigma-*T* values from a MARMAP site near the Hudson Canyon showing the pycnocline's seasonal cycle in the area.

storms that have cooled the water and thoroughly mixed it. With the advent of spring, the storms cease and strong solar heating causes a seasonal thermocline to develop and deepen from May to September. It is during this part of the year that internal waves exist due to the presence of a pycnocline at a mean depth of about 20–25 m. The internal waves are generated by the interaction of the tidal currents with the shelf break as shown by Lamb (1994). The density at the surface ranges over five sigma-*T* values, whereas the density at the bottom ranges over about one sigma-*T* value over most of the year. Thus the variance between observation and climatology is smaller in the bottom layer.

Figure 3 is the southern SAR image centered at approximately 39.6°N, 72.6°W. The image is roughly 100 km × 100 km square. Note that there are no internal waves in the lower-right portion of the image and only rather weak indications of their existence in the upper-left portion. Moving from the lower-right corner of the image diagonally to the upper-left corner, internal wave generation, propagation, and dissipation can be observed. There are four strong packets of waves in the lower center of the image. This image shows that wave genesis and dissipation takes place over a distance of roughly 100 km across the continental shelf.

As was pointed out previously, the generally accepted hypothesis is that the interaction of the internal tides with the sharply sloped bathymetry at the shelf break is the dominant generation mechanism for internal waves. This hypothesis is consistent with these observations that show no internal waves east of the shelf break (indicated by 200-m isobath in Fig. 1) near the lower-right (southeast) corner of the image. The bright features just to the northwest of the shelf break could, in fact, be a manifestation of internal wave signature generation.

The region of the shelf break also appeared to be the generation region for internal waves seen in photographs taken from the space shuttle in 1991 (Zheng and Klemas 1993). Waves located farther inshore of the linear packet seen in Fig. 3 begin to exhibit more circular wave fronts, still roughly following the bottom topography.

There are a number of physical mechanisms that may be responsible for the change in the shape of the wave packets. Some are 1) effects of the bottom topography, 2) horizontal variation of the water-column stratification along the propagation path, 3) the advection of the waves by variable current fields along the propagation path, 4) variations in the direction of the tidal forcing from one cycle to the next, and 5) variations of wind and wave fields that can also cause changes in the surface signatures.

Jones (1995) attempted to use SAR images to monitor the Brunt–Väisälä frequency. He proposed using Fourier transforms and estimated that to compute the modal dispersion relation with a 15% or less error, 17 h of observations would be necessary to obtain one profile

FIG. 3. *ERS-1* SAR image from 18 July 1992 that is a 100 km × 100 km square. Note that the four strong packets of internal waves are clearly seen in the lower center of the image.

over a 200 km^2 area. He concluded that this was not a practical method for estimating the density structure of the water column. Here we propose a simplified but more robust method to estimate the density structure of the water column on the continental shelf.

In this study, we use a simple two-fluid model with the assumption that the internal waves break when the two layers have comparable depth. By using climatological data to estimate the stable bottom density, knowledge of the frequency of the wave generation (i.e., the tidal period), and the dispersion relation for a two-layer fluid, we are able to estimate the depth and density of the thermocline.

2. Background

Our basic assumptions about the internal waves observed in the SAR image shown above are that they are generated every tidal cycle (i.e., every 12.42 h), that they propagate on the interface of a two-layer fluid, that the bottom density of the water column is represented accurately by the climatological data, and that the waves begin to dissipate when the depths of the two fluids are comparable.

The tides generate soliton waves as the internal tide impinges on the continental break. Lamb (1994) has shown a numerical model demonstrating this wave-generating mechanism. In a recent study of internal waves generated at the continental shelf break (Chapman 1998) it was shown that wave packets could be generated on the flood tide without invoking lee waves as Lamb did. In any case, the fact remains that the internal waves are generated at tidal cycles.

Our simple two-layer model consists of a surface layer of depth h_1 and a bottom layer of depth h_2. We also assume that the depth changes on a length scale that is much larger than that of the internal waves. The model is shown schematically in Fig. 4. The controlling equation is

$$\nabla^2 \phi_l = 0 \qquad l = 1, 2, \tag{1}$$

where $\phi_l(x, z, t)$ is the streamfunction in layer l. The boundary conditions are

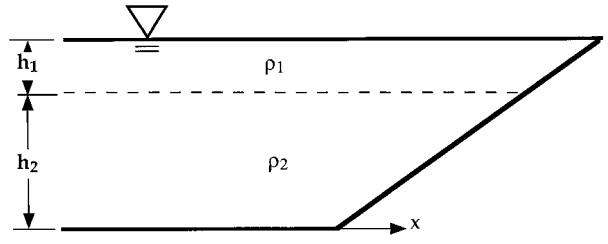

FIG. 4. Schematic of our two-layer model. The dashed line shows the interface between the top and bottom fluids.

$$\frac{\partial \phi_1}{\partial z} = \frac{\partial \eta}{\partial t}, \qquad \text{at } z = 0, \tag{2a}$$

$$\frac{\partial \phi_1}{\partial t} + g\eta = 0, \qquad \text{at } z = 0, \tag{2b}$$

$$\frac{\partial \phi_1}{\partial z} = \frac{\partial \phi_2}{\partial z} = \frac{\partial \zeta}{\partial t}, \qquad \text{at } z = -h_1, \tag{2c}$$

$$\rho_1\left(\frac{\partial \phi_1}{\partial t} + g\zeta\right) = \rho_2\left(\frac{\partial \phi_1}{\partial t} + g\zeta\right), \quad \text{at } z = -h_1, \tag{2d}$$

and

$$\frac{\partial \phi_2}{\partial z} = 0, \quad \text{at } z = -h_1 - h_2, \tag{2e}$$

where $\eta(x, t)$ is the free surface displacement, $\xi(x, t)$ is the displacement at the interface, ρ_l is the density in layer l, and g is the acceleration of gravity. Equations (2a)–(2e) specify two distinct dispersion relations; one is related to the wave motion at the free surface (i.e., surface waves) and the other is related to internal-wave motion at the density interface. The latter dispersion relation is of interest to us in this study. We specify it here in schematic form as

$$\omega^2 = f(g, k, h_1, h_2, \rho_1, \rho_2), \tag{3}$$

where the function f represents the rather complicated dependence on the layer depths and densities as well as k (and g). The solid curves in Fig. 5 show this dispersion relation plotted as a function of k for two different two-layer configurations. The left-hand plot is computed for an upper-layer thickness $h_1 = 20$ m and a lower-layer thickness $h_2 = 180$ m, while in the right-hand plot, $h_1 = 20$ m and $h_2 = 50$ m. For both plots in Fig. 5, the density in the upper layer is $\rho_1 = 1.022$ g cm^{-3}, and in the lower layer it is $\rho_2 = 1.025$ g cm^{-3}. The range of k values shown in these plots corresponds to wavelengths greater than about 100 m (for $k = 0.06$ rad m^{-1}). What we want to show in Fig. 5 is the sensitivity of our two-layer dispersion relation to changes in the lower-layer depth for a fixed depth of the upper layer. The configuration shown in the left panel of the figure corresponds to a region near the shelf break, while the right panel corresponds to a region farther inshore. One can see from this figure that the dispersion curves have the same general form, but in the case of the shallower bottom layer, the frequency is somewhat lower and more linear over the range of k values shown.

As mentioned above, the analytical form of the two-layer dispersion relation is rather complicated. For cases where $k(h_1 + h_2) \ll 1$ *and* $|(\rho_2 - \rho_1)/\rho_1| \ll 1$, this relation may be simplified considerably. For these conditions, one may expand the function f in (3) in powers of kh_1, kh_2, and $(\rho_2 - \rho_1)/\rho_1$. The leading terms in this

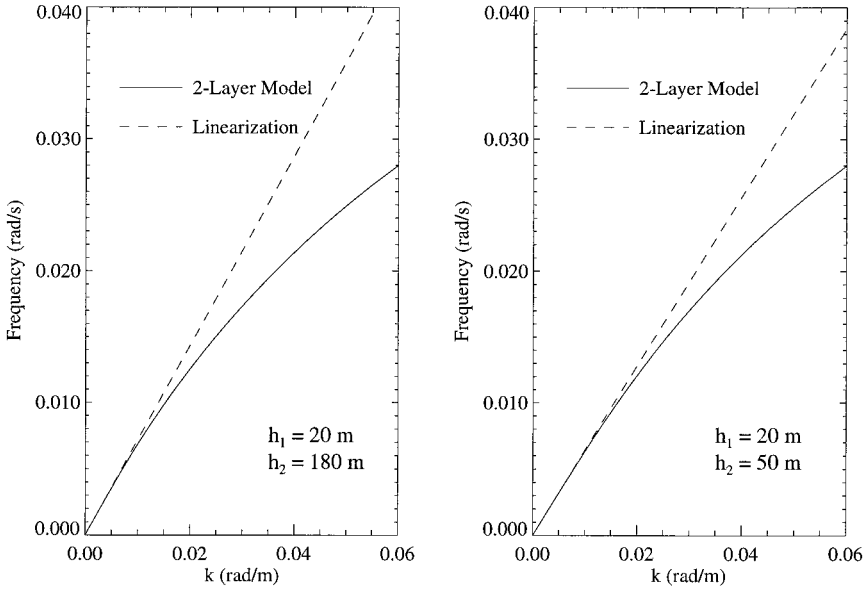

FIG. 5. Plot of the two-layer dispersion relation (solid curves) and a long-wavelength small-density-difference approximation (dashed curves). In the left-hand plot, the layer depths are $h_1 = 20$ m and $h_2 = 180$ m, while in the right-hand plot, $h_1 = 20$ m and $h_2 = 50$ m.

expansion turn out to be quadratic in k and linear in $(\rho_2 - \rho_1)/\rho_1$. Retaining only these leading-order terms, we obtain an expression for ω, call it ω_0, that is linear in k. The dependence of ω_0 on k for both two-layer systems is shown by the dashed curves in the corresponding panels in Fig. 5. The linear approximation for ω is valid for wavenumbers less than about 0.02 rad m^{-1} (or wavelengths greater than about 300 m) for both systems with the approximation being somewhat more accurate for the shallower bottom layer. The lead waves in the internal wave packets seen in Fig. 3 have wavelengths of this order (Porter et al. 1993).

The phase speed, C_{p0} $(=\omega_0/k)$, corresponding to ω_0 obtained from this linearization is independent of k and depends only on the layer depths and densities. The form for C_{p0} is given by

$$C_{p0} = \sqrt{g\frac{(\rho_2 - \rho_1)}{\rho_2}\frac{h_1 h_2}{(h_1 + h_2)}}. \tag{4}$$

The value of C_{p0} for the case of the deeper lower layer is 0.72 m s^{-1}, while that for the shallower lower layer is 0.64 m s^{-1}. These values are in general agreement with the phase speeds measured during JUSREX (Porter et al. 1993). Since the lead waves in Fig. 3 are in fact nonlinear solitons, their phase speeds will generally be somewhat higher than those predicted by a simple two-layer model. Therefore, using (4), which provides an upper bound on the two-layer phase speed computed from ω/k using (3), will at least partially compensate for this effect. We will see below that use of the simple expression for the phase speed of the internal waves in terms of the layer depths and densities given by (4) can be a useful tool for estimation of various properties of the water column.

At the northeastern edge of Fig. 3, the internal-wave signatures appear significantly weaker than in other regions of the image. We believe the internal waves are dissipating in this region. A number of numerical studies (Helfrich and Melville 1986; Helfrich 1992; Saffarinia and Kao 1996; Porter et al. 1993) have shown that as the internal soliton approaches a sloping bottom, the wave begins to reverse its shape and break. Other phenomena can affect the depth at which the internal-wave signature disappears. These include bottom friction dissipation, local internal-wave breaking, and local Richardson instabilities. Saffarinia and Kao (1996) have shown that when only the depth ratio between the top and bottom layer is important, instabilities occur when the depths of the top layer and the bottom layer are equal. Thus, if we assume, based on laboratory and computer models, that the waves probably break and dissipate when the depths of the two layers are equal, then the disappearance of the internal-wave's surface signature in the SAR imagery will correspond to that condition. We should be able to check the consistency of this assumption with the observations made from the SAR. In order to do this, we can use the climatological data base to estimate the bottom density ρ_2, obtain the total depth of the water column where the waves dissipate from bathymetry charts, and deduce the internal-wave phase speed from the SAR image. These quantifies can then be used to solve (4) for the upper-layer density ρ_1. In the following discussion, we will show that these assumptions in fact appear to be sound.

3. Observations

The SAR image shown in Fig. 3 was collected on 18 July 1992 in the New York Bight area of the eastern coast southeast of Long Island by the *ERS-1* satellite. This satellite operates at a frequency of 5.3 GHz (C band) at vertical polarization with a nominal resolution of 25 m and a swath width of 100 km. The incidence angle at the swath center is 23°. The imagery shown in these figures is 100 km on a side and has been obtained by smoothing the full-resolution data to 150-m pixels. Since the 5.3-GHz microwaves ($\lambda \approx 0.056$ m) from the SAR penetrate only a few centimeters into the surface, it is clear that the features in the image must be caused by a surface manifestation of the internal waves. Furthermore, we know that the surface displacement arising from the internal wave's passage is much too small to cause the observed modulation on the SAR intensity. It is, in fact, the variable surface–current field generated by the internal waves that is ultimately responsible for their visibility in the SAR image. Qualitatively, the internal-wave surface current modulates the surface-wave spectrum as a function of position across the internal-wave phase. This modulation produces a differential surface roughening that causes the corresponding change in the SAR intensity that is seen in the imagery. For a more detailed discussion of this wave–current interaction process, see, for example, Thompson et al. (1988) as well as other papers in JOWIP and SARSEX Special Issue (1988).

The generation mechanism for these internal waves is assumed to be the interaction of the internal tides with the steeply sloping bottom topography of the continental break (Lamb 1994). The internal waves appear to consist of packets (or trains) of solitons. Solitons are nonlinear waves that can be described by a solution to the Korteweg–de Vries (KdV) equation (Gasparovic et al. 1988). The waves in these wave packets are rank ordered by amplitude with the lead wave being the largest. Because the phase speed of a soliton is proportional to its amplitude, the distance between the waves in the packet is also rank ordered from the front to back; the lead waves outrun the smaller waves behind them.

Let us examine these waves more closely. Figure 6 shows a closeup of the genesis area of these internal waves. (The exact position of this image is the region of circle number 2 in Fig. 11.) The image has been rotated so that the wave crests are vertical, and the area between the two thin horizontal white lines has been vertically averaged to give a measure of the intensity

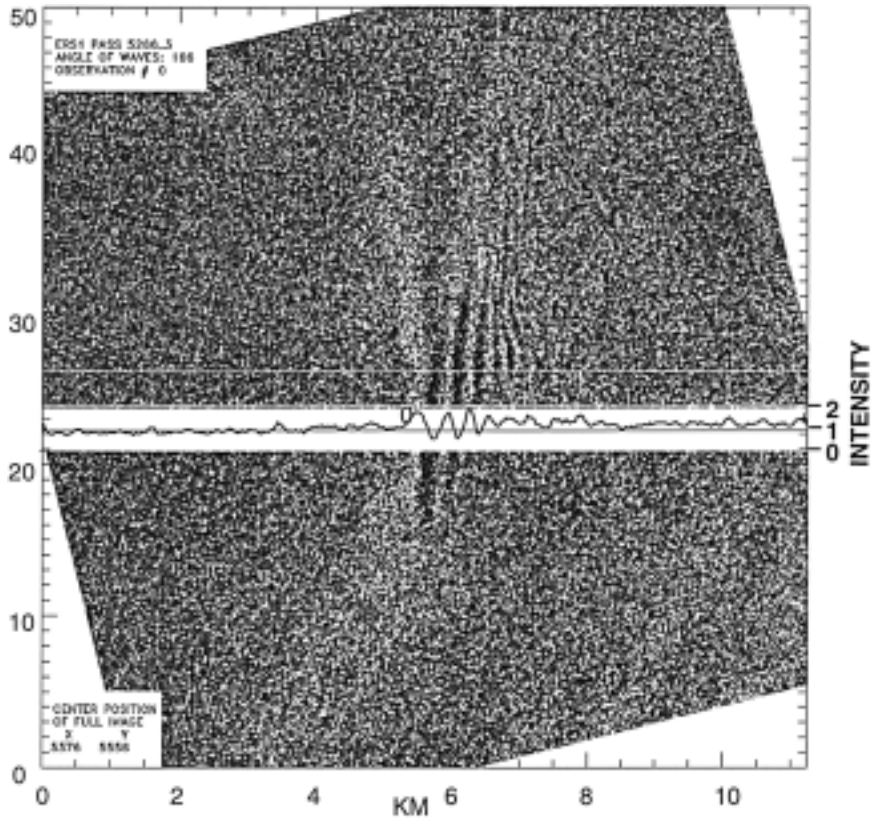

FIG. 6. An image showing the genesis of the internal waves right at the shelf break (circle 2 in Fig. 11). The figure was rotated so that the transect across the waves was normal. Note the two parallel horizontal lines in the image. The intensity was averaged vertically between these two lines and is plotted as a black line in the white strip below the two parallel lines.

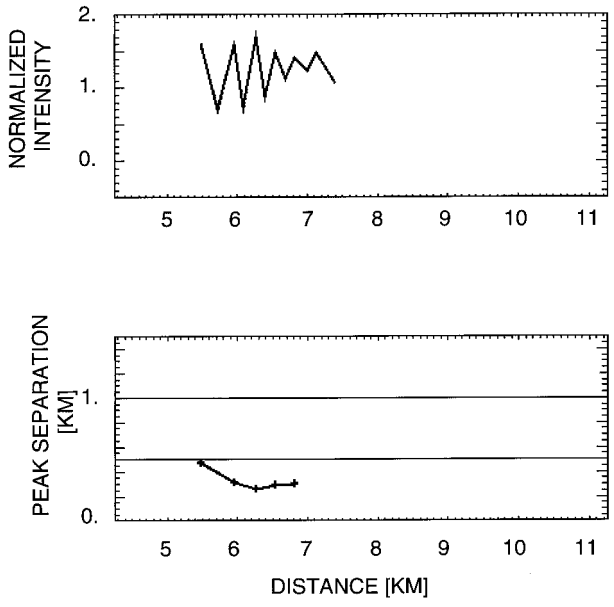

FIG. 7. Plotted are the extrema of the single plot shown in Fig. 6 vs distance. The top panel shows the crests and troughs of the intensity curve, and the bottom curve shows the calculated separations.

of the waves. This was plotted in the white space directly below the area marked by the thin white lines. There are 41 pixels between the two white lines, corresponding to a width of about 6 km. The single line plot shows the normalized wave intensity of the waves. The average intensity of the area ahead of the wave signature from about 0 to 5 km was used to compute the normalization factor. Thus, the normalized intensity has a value of 1 when it is equal to the background. This method is used in Figs. 6 and 8 to compute intensity cuts through the wave packet.

The positions of the crests and troughs of the waves shown in the single line plot in Fig. 6 are plotted in the top panel of Fig. 7. Note that there are three large waves followed by two smaller ones. We calculated the distance from crest to crest and plotted the separation for these five waves in the bottom panel of Fig. 7. The distance between the leading waves is about 0.5 km and decreases to a value of about 0.35 km for the waves at the end of the train.

Figures 8 and 9 were analyzed for circle 10 in Fig. 11, in the same manner as Figs. 6 and 7. Note that a single crest in a packet of waves extends well over 50 km and that there appear to be about 10 internal waves

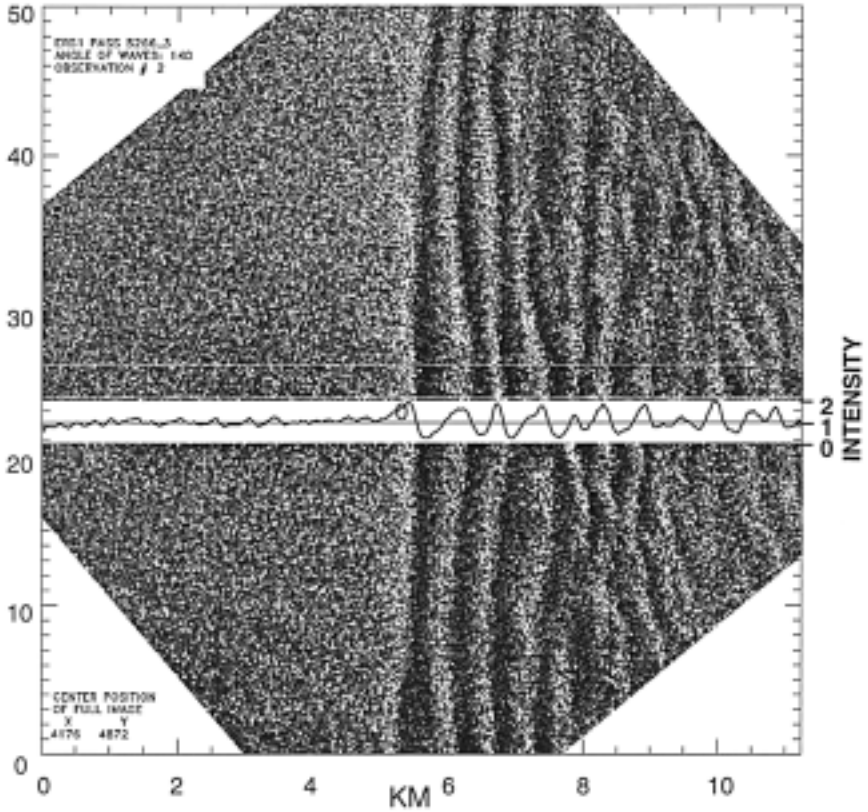

FIG. 8. An image showing the internal waves inshore of the shelf break (circle 10 in Fig. 11). The figure was rotated so that the transect across the waves was normal. Note the two parallel horizontal lines in the image. The intensity was averaged vertically between these two lines and is plotted as a black line in the white strip below the two parallel lines.

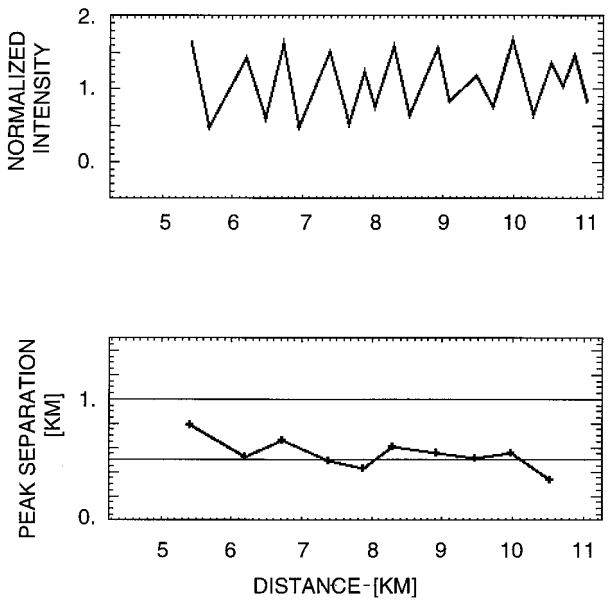

FIG. 9. Plotted are the extrema of the single plot shown in Fig. 8. The top panel shows the crests and troughs of the intensity curve and the bottom curve shows the calculated separations.

in the internal wave train. The first wave has a separation of about 0.8 km with all the other separations being approximately 0.6 km. We assume that these waves propagate all the way from the shelf break to the shallows, where they begin to dissipate in water that is approximately 55 m deep.

If we assume that the waves shown in Fig. 8 had their genesis at the same location as the waves in Fig. 6, we see from Fig. 9 that the waves start off with a separation of about 0.5 km and that the leading wave separation grows to 0.8 km with the number of waves in the wave train increasing in number and in separation. These images are similar to the wave packets shown in Fig. 6 of a paper by Helfrich and Melville (1986). They investigated a two-layer fluid and used the KdV equations to model the waves running up onto a sloping bottom, as shown in Fig. 4. In their figure they show a soliton wave approaching the slope. As it impinges on the slope, the wavelength of the leading wave becomes larger and a train of internal waves develops behind the lead wave. This behavior is very similar to that of the internal waves that we observed from the SAR.

Figure 10 shows the northern SAR image that is outlined in Fig. 1. Along a transect running from the southeast corner to the northeast corner, we computed the

FIG. 10. Image showing the wave direction computed using the Radon method.

Radon transform (Murphy 1986). This procedure provides an estimate of the dominant direction of the wave crests. The white lines shown in Fig. 10 are perpendicular to the wave crests determined in this manner. One should note that at the three positions in the image where the transform was computed on internal-wave crests, the resulting propagation directions are almost collinear. When the location of the Radon transform does not coincide with wave crests, the directions are highly variable. Thus, it appears that these wave packets are generated at the same site and travel along similar paths. This gives credence to the hypothesis that these wave trains were generated at the same shelf feature and allows us to compute the speed of the waves from the feature separation observed in the image.

From Fig. 3 we have seen that as the internal waves travel into shallow water they appear to dissipate. As mentioned earlier, there is evidence that this dissipation occurs when the depth of the pycnocline is half the total depth of the water column. We now want to quantitatively ascertain from SAR imagery the depth at which this dissipation occurs. To accomplish this measurement, we have made 82 observations at the locations of the circles shown in Fig. 11. The water depth was taken from the bathymetry as shown in this figure. Each observation circle has a diameter of 5.4 km. All of the observation circles are placed along the propagation direction of the internal waves except for circles 1 and 82, which are in the deepest and shallowest waters, respectively, where no internal wave signals appear. In each circle we compute the mean depth and also the variance of the intensity of the microwave backscatter in the circle. Thus, circles 1 and 82, which are a uniform shade of gray, have a very small variance, whereas circle 9, which contains a set of very intense internal waves, has a large variance. We normalized the variance in each circle by that found for circle 82. This normalized variance is then a quantifiable measure of the strength of the waves at the locations specified by the circles in the image.

In addition to the 82 circles from Fig. 11, we have also computed the normalized variance in the circles along the internal-wave transect shown in Fig. 12, which is the northern image of Fig. 3. (The variance for this case is normalized by that in circle 17.) Note in Fig. 12 that the bottom topography does not contain the large irregularities associated with Hudson Canyon, which is located in the region covered by Fig. 11 and which the bathymetry slowly shoals toward the upper-left corner of the image.

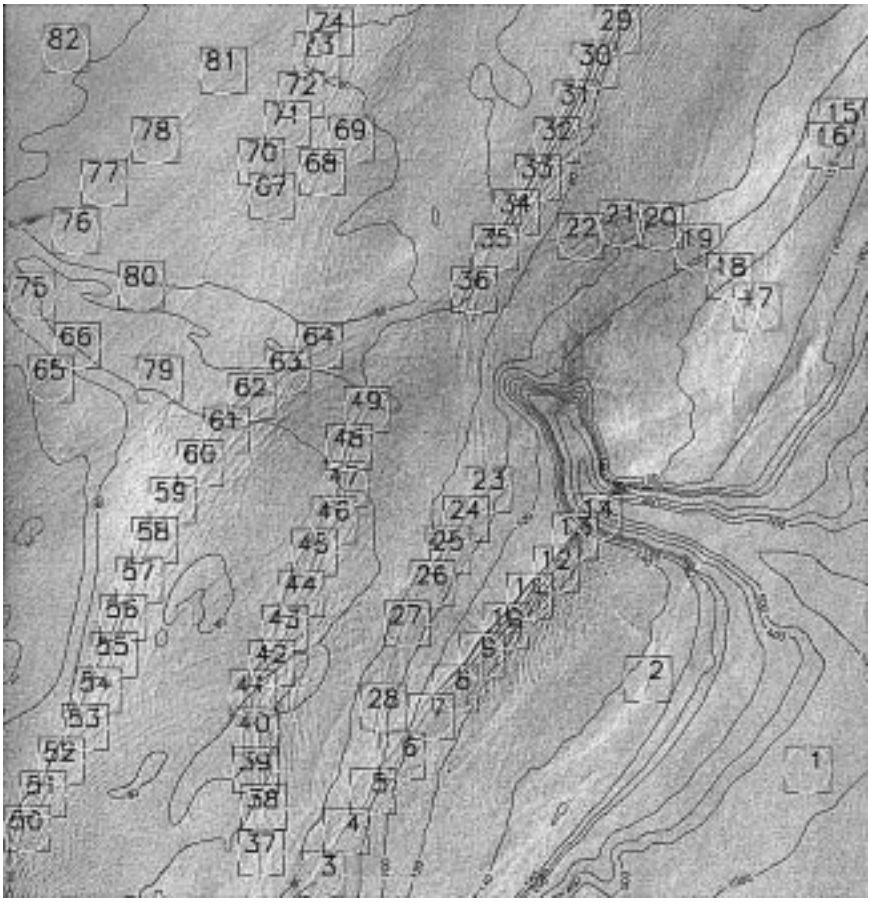

FIG. 11. The SAR image with the bottom topography on as well as the observation circles.

Figure 13 shows a plot of the normalized intensity variance versus depth for Figs. 11 and 12. The top panel shows the transect from Fig. 12. Note that the variance is greater than 1 until the depth reaches a value of about 55 m. Similarly, in the bottom panel we see that the normalized intensity variance is generally greater than 1 until about 55 m. There are some cases with a depth greater than 55 m where the intensity of an observation is less than unity. These cases are probably more a result of the particular placement of the circle than of a systematic decrease in the normalized intensity variance. An example would be circle 26, which has a small variance due to the position of the internal waves within the circle. For depths shallower than 55 m, however, the normalized intensity variance remains at a value of unity or less.

Note that in both panels in Fig. 13 the normalized intensity variance drops to 1 or below at a depth of 55 m. If we assume that this is the depth where the solitons begin to break and dissipate, then, based on the previously cited numerical and laboratory experiments, this is the depth where the pycnocline depth equals the depth beneath the pycnocline, that is, both depths are about 27.5 m. Unfortunately, there were no simultaneous observations of the water column in the shoaling area corresponding to the satellite overpass shown in Figs. 11 and 12. However, to the northeast of the Hudson Canyon (40.2°N, 71.9°W), the R/V *Ioffee* was towing a conductivity, temperature, and depth (CTD) profiler (Porter et al. 1993). Measurements of the water column from that instrument show a broad pycnocline extending from a 15- to 25-m depth in water about 60 m deep. This is in the range where the waves should become unstable and break.

Thus, if we know the bathymetry and can pinpoint where the waves dissipate, then we have an estimate for the depth of the thermocline without taking measurements in the water column. The next question is whether we can further use this information to infer the density difference between the two layers.

Since the southern image (Fig. 11) contains irregular bottom topography that renders the internal-wave field to be very chaotic and hard to interpret, we will concentrate on the northern SAR image from Fig. 12 in our attempt to extract the density difference between the layers. If we know that the wave crests in this image are one tidal cycle apart (i.e., 12.42 h) and measure the distance between the wave packets, we can estimate

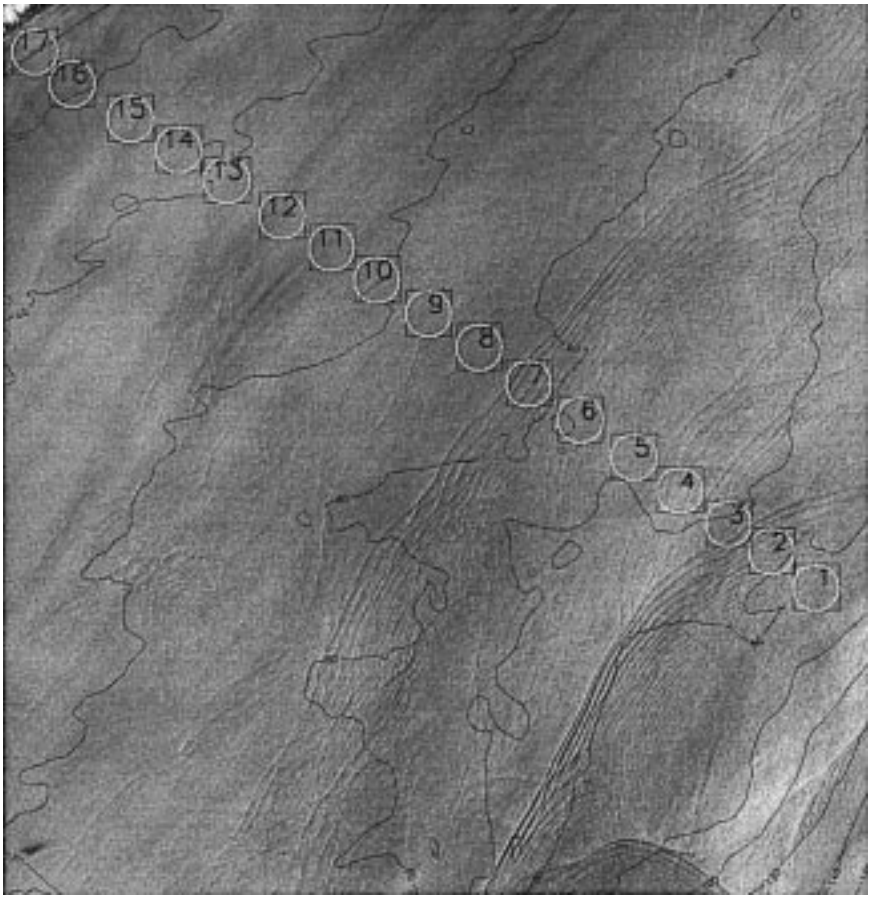

FIG. 12. Image collected on 18 July 1992 showing the scene just to the north of that in Fig. 3. In the upper-left corner is a small piece of Long Island. The depth and variance was calculated for each circle in the transect.

their speed of propagation. In Fig. 14, which shows the same northern image as Fig. 12, we show nine lines equally spaced along the wave crests of two internal-wave trains whose generation time is assumed to be separated by 12.42 h. We have averaged the length of the nine lines and divided that by the tidal cycle period to obtain a speed of 0.62 ± 0.01 m s^{-1}. The error quoted here includes only our estimate of the uncertainty associated with connecting corresponding points on the two wave trains. Besides these errors, there are clearly systematic errors caused by currents on the shelf and horizontal variability of the density field. It is therefore not surprising that observations from moorings on the shelf by Colosi et al. (1997) and Lynch et al. (1997) show that the arrival of solibores on the shelf do not occur at exactly 12.42-h intervals.

Based on these and other observations, we will assume for our analysis that the solibores are generated at 12.42 h with an ambiguity on the order of about 10%. This phase speed estimate of 0.62 ± 0.06 m s^{-1} is within the range of speeds observed in the New York Bight by Liu (1988).

What does this information tell us about the density structure of the water column? As mentioned previously, we have CTD measurements, conducted during JUSREX, that characterize the density structure of the imaged area. At the time of the image in Fig. 14, the depth of the pycnocline in the region between the two internal-wave packets was in the 20-m range with a bottom-layer density of 1.0253 g cm^{-3} and an upper-layer density of 1.0224 g cm^{-3}. Thus, the density difference between the two layers was 0.0029 g cm^{-3}.

We now want to see how this value compares with that inferred using our estimate of the internal-wave phase speed in conjunction with (4). We review again the steps in this procedure. 1) The total depth at the position where the internal waves no longer appear in the SAR image was determined from bathymetry to be about 55 m. With the assumption that in a two-layer regime, the waves dissipate when the layer depths are equal, we deduce layer depths of 27.5 m at this position. 2) A further assumption is that the upper-layer depth remains roughly constant over the entire region from shelf break to the dissipation location. 3) The bathymetry at the position where the internal-wave phase speed is measured from the imagery (as discussed above in

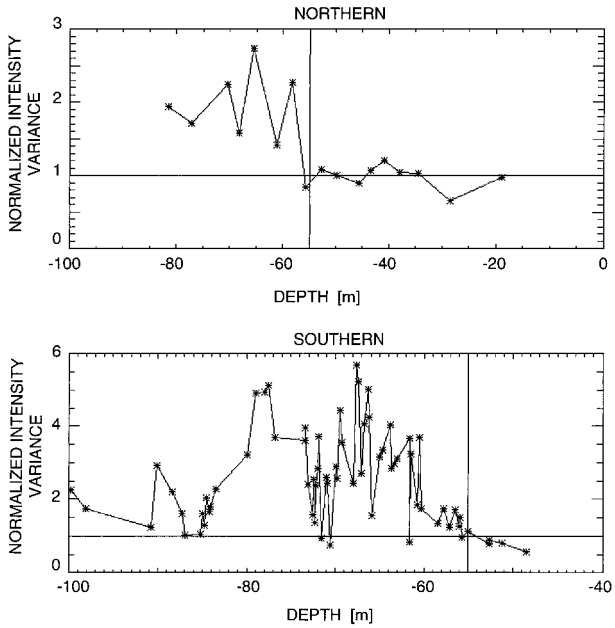

FIG. 13. Normalized intensity variance vs depth. The upper panel shows the results from the northern image (Fig. 12), and the bottom panel shows those for the southern image (Fig. 11).

conjunction with Fig. 14) then implies the lower-layer depth at this location. For the present case, the depth at the phase-speed measurement location is 65 m, which implies a bottom-layer depth of 37.5 m. 4) We may now use the linearized phase-speed equation (4) to determine the fractional density change, $(\rho_2 - \rho_1)/\rho_1$, between the two layers, or, if the lower-layer density is known (e.g., from climatology), the absolute upper-layer density.

The left panel in Fig. 15 shows plots of the phase speed versus the density fraction $(\rho_2 - \rho_1)/\rho_1$ computed using (4). The solid curve in this panel was computed using our best estimate of the layer depths; namely, $h_1 = 27.5$ m and $h_2 = 37.5$ m. The other two curves give an indication of the sensitivity (4) to changes in these depths. The dashed curve was computed using $h_1 = h_2 = 32.5$ m, while for the dotted–dashed curve, $h_1 = 22.5$ m and $h_2 = 42.5$ m were used. Note that for both cases, the total depth $(=h_1 + h_2)$ is held constant. We thus can see that a $\pm 10\%$ change in the upper-layer depth corresponds roughly to a $\pm 8\%$ error in the density fraction. The right-hand panel of Fig. 15 is similar except that it shows phase speeds computed using the full two-layer dispersion relation corresponding to an internal-wave wavelength, λ, of 300 m. We see from the curves in this panel that the error bound of the density fraction is a bit tighter for this case. (As λ becomes large, of course, the curves in the right panel become identical to those in the left.) Therefore, for cases where a reasonably accurate estimate of λ can be made, a somewhat more precise value for the density fraction can, in principle, be obtained by solving for this quantity using the full dispersion relation.

If we take the value of $\rho_2 = 1.0253$ g cm^{-3} measured during JUSREX, the density difference from the linearized phase-speed estimate in Fig. 15 yields an upper-layer density of $\rho_1 = 1.0228$ g cm^{-3} in good agreement with the estimated value of 1.0224 g cm^{-3}. The ρ_1 value obtained using the full dispersion is in even better agreement with the measurement, but this is probably somewhat fortuitous since the wavelength of the lead solitons appears to be somewhat larger than 300 m.

There are, of course, several caveats that need to be stressed in connection with discussion presented above. First, one must keep in mind that SAR observations are time limited. This means that an estimate of the location of the dissipation region may be in error simply because the waves have not yet propagated farther onto the shelf at the time of the image. This usually results in an overestimate of the critical depth (and the pycnocline depth). Also, there will certainly be cases when the water column is not well characterized as a simple two-layer system. Especially near the shelf break, for example, a thin but well-defined bottom layer is sometimes observed below the usual two-layers typical of the region farther inshore (Lynch et al. 1997). We have briefly investigated the effect this type of stratification on the density-fraction estimate using the dispersion relation derived from a three-layer model. We have found that if the thickness of the bottom layer is thin ($\leq 10\%$ of the total depth of the water column), and its density is ≤ 0.005 g cm^{-3} larger than the midlayer, then the computed density fraction for the example discussed above is within a few percent of that found for the two-layer case. A more prominent bottom layer will, of course, give rise to larger changes.

4. Conclusions

We have shown in this paper how it may be possible to remotely estimate various properties of the water column on the continental shelf using SAR imagery in conjunction with knowledge of the local bathymetry, climatological density data, and simple models for internal-wave evolution. Theoretical studies of two-layer fluids indicate that dissipation of internal waves impinging on shoaling water occurs when the depth of the bottom layer, which is decreased by the shoaling, becomes equal to that of the upper layer. Using this idea, we have determined this critical depth for a particular case study by noting the location in the SAR image where the internal-wave surface signatures disappear. The depth of each layer at this position is then half the total depth. By assuming that the internal waves are generated at the shelf break on each diurnal tidal cycle, we have also estimated their phase speed by measuring the distance between successive packets in the image. With this information along with the two-layer dispersion relation, we have been able to estimate the fractional density change between the two layers. Furthermore, an estimate of the surface density is possible by

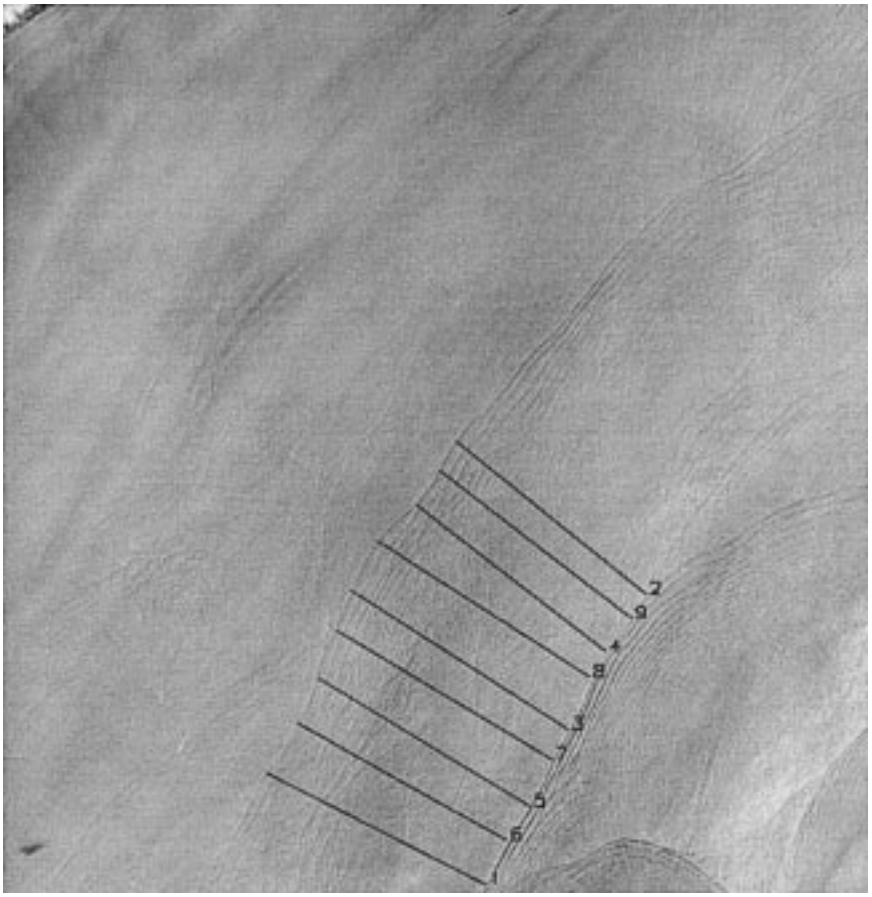

FIG. 14. Image of 18 July 1992 north of the image shown in Fig. 3. The upper-left corner shows a small section of the south shore of Long Island.

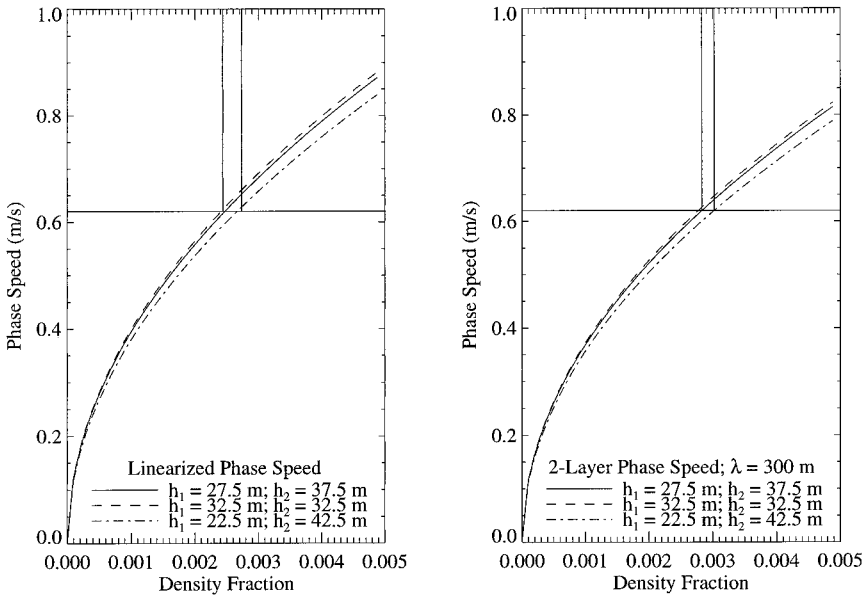

FIG. 15. Phase speed vs density fraction computed from linearized relationship (left panel) and full two-layer dispersion relation (right panel) for several combinations of layer depths. The horizontal line shows where a phase speed of 0.62 m s^{-1} intersects the various curves, and the vertical lines indicate the error bounds on the density fraction corresponding to the depth variations.

using the climatological bottom density. We have compared the parameters extracted using these methods with in situ measurements collected concurrently with the SAR imagery. This comparison showed good agreement and gives us confidence that our techniques are robust.

There are, of course, many refinements that will certainly improve the remote-sensing extraction techniques discussed above. As mentioned earlier, knowledge of the internal-wave wavelength would allow one to estimate the fractional density change more accurately. Nonlinear corrections to the phase speed of the solitons could also be applied. These refinements are presently being investigated using imagery and in situ data obtained during the ONR-sponsored Coastal Mixing and Optics Experiment. The robustness of the techniques described in the present paper gives us confidence that such efforts are worthwhile and such remote sensing techniques will eventually become common tools for coastal oceanography.

Acknowledgments. This study was supported by the Office of Naval Research (N00014-95-1-0077 and N00014-96-1-0835). We thank Dr. James Lynch of Woods Hole Oceanographic Institution and another (anonymous) reviewer for very helpful comments and suggestions. We also thank Dr. Richard Gasparovic of The Johns Hopkins University Applied Physics Laboratory for his useful discussions.

REFERENCES

Chapman, R., 1998: Generation and evolution of internal waves in the New York Bight during the 1992 joint U.S./Russia Internal Wave Remote-Sensing Experiment. *Eos, Trans. Amer. Geophys. Union,* **79,** 177.

Colosi, J., C. Rehmann, and J. Lynch, 1997: Just how stochastic are coastal oceanographic fields? *J. Acoust. Soc. Amer.,* **102** (5), Pt. 2, 3081.

Gasparovic, R. F., 1992: Joint U.S./Russia Internal Wave Remote Sensing Experiment Wallops operations report. JHU/APL Tech. Rep. S1R-92U-033, 54 pp.

——, J. R. Apel, and E. S. Kasischke, 1988: An overview of the SAR Internal Wave Signature Experiment. *J. Geophys. Res.,* **93** (12), 304–316.

Gotwols, B. L., R. E. Sterner II, and D. R. Thompson, 1988: Measurement and interpretation of surface roughness changes induced by internal waves during the Joint Canada–U.S. Ocean Wave Investigation Project. *J. Geophys. Res.,* **93** (12), 265–282.

Helfrich, K. R., 1992: Internal solitary wave breaking and run-up on a uniform slope. *J. Fluid Mech.,* **243,** 133–154.

——, and W. K. Melville, 1986: On long nonlinear internal waves over slope-shelf topography. *J. Fluid Mech.,* **167,** 285–308.

Jones, R. M., 1995: On using ambient internal waves to monitor Brunt–Väisälä frequency. *J. Geophys. Res.,* **100** (6), 11 005–11 011.

JOWIP and SARSEX Special Issue, 1988: *J. Geophys. Res.,* **93** (C10), 12 217–14 164.

Lamb, K. G., 1994: Numerical experiments of internal wave generation by strong tidal flow across a finite amplitude bank edge. *J. Geophys. Res.,* **99** (1), 843–864.

Liu, A. K., 1988: Analysis of nonlinear internal waves in the New York Bight. *J. Geophys. Res.,* **93** (10), 12 317–12 329.

Lynch, J. F., and Coauthors, 1997: Shelfbreak PRIMER—An integrated acoustic and oceanographic field study in the middle Atlantic bight. *Shallow Water Acoustics,* R. Zhang and J. Zhou, China Ocean Press, 205–212.

Manning, J., and T. Holzwarth, 1990: Description of oceanographic conditions on the northeast continental shelf: 1977–1985. Northeast Fisheries Center Reference Doc. 90-04, 373 pp. [Available from NOAA/National Marine Fisheries, Northeast Fisheries Center, Woods Hole, MA 02545.]

Murphy, L. M., 1986: Linear feature detection and enhancement in noisy images via the Radon transform. *Pattern Recognition Lett.,* **4,** 279.

Porter, D. L., and D. R. Thompson, 1996: Estimation of thermocline depths from SAR imagery and a two-layer density model. *IGARRSS 96,* **II,** 1152–1154.

——, R. D. Chapman, and R. F. Gasparovic, 1993: Comparisons of internal waves as observed by a towed CTD and radar images. JHU/APL Tech. Rep. S1R-93U-010, 27 pp.

Saffarinia, K., and T. W. Kao, 1996: A numerical study of the breaking of an internal soliton and its interaction with a slope. *Dyn. Atmos. Oceans,* **23,** 379–391.

Thompson, D. R., B. L. Gotwols, and R. E. Sterner II, 1988: A comparison of measured surface-wave spectral modulations with predictions from a wave–current interaction model. *J. Geophys. Res.,* **93** (C10), 12 339–12 343.

Zheng, X.-H., and V. Klemas, 1993: Statistical and dynamical analysis of internal waves on the continental shelf of the middle Atlantic bight from space shuttle photographs. *J. Geophys. Res.,* **98** (C5), 8495–8504.